♦Track Deflection of Typhoon Nesat (2017) as Realized by Multiresolution Simulations of a Global Model

CHING-YUANG HUANG AND CHIEN-HSIANG HUANG

Department of Atmospheric Sciences, National Central University, Jhong-Li, Taiwan

WILLIAM C. SKAMAROCK

National Center for Atmospheric Research, Boulder, Colorado

ABSTRACT

Typhoon Nesat (2017) headed west-northwestward toward Taiwan but took a relatively larger northward deflection about 300 km away and then a leftward deflection after landfall at northern Taiwan. A global model MPAS, employing a multiresolution of 60–15–3 km mesh, is used to investigate the underlying mechanisms of the track changes. The global model simulations are capable of resolving the detailed topographical effects of the Central Mountain Range (CMR) in Taiwan, giving reasonable 5 day tracks in agreement with the observations for Typhoons Soudelor (2015) and Megi (2016), and comparing better with the observed deflection of Nesat (2017) than the regional model simulation of WRF. Sensitivity experiments indicate that flattening the CMR only partially reduces the track deflection of Nesat, while the elimination of the initial cyclone over the South China Sea disables the possible Fujiwhara effect and leads to a southward-biased track with much weaker northward deflection. The northward deflection of Nesat is mainly in response to the wavenumber-1 (WN-1) horizontal PV advection as the southerly flow east of the typhoon center is enhanced by convergence with the outer cyclonic typhoon flow and the large-scale southwesterlies. Upward motions and PV in the troposphere thus are much stronger to the east of the center than to the west, resulting in westward translation induced by negative WN-1 vertical PV advection but eastward translation induced by positive WN-1 vertical differential latent heating to the east. Near landfall, with stronger upward motions produced over the northern CMR, vertical differential latent heating averaged in 3–8-km height becomes negative and thus retards the westward translation.

1. Introduction

Some of the most striking orographic influences on an impinging tropical cyclone (TC) are track changes evolving over free oceans and near an obstacle with high orography. A cyclonic path of the track around the northern corner of the mountain ridge was first noticed when a westbound tropical cyclone (TC) approached the northern sector of the mountain ridge (e.g., Wang 1980; Chang 1982). Many numerical studies have been devoted to investigating the intriguing track evolution for idealized TCs over a bell-shaped mountain or realistic mountains like the Central Mountain Range (CMR) in Taiwan that is elongated mainly north-southward with a maximum height over 3500 m (e.g., Chang 1982; Bender et al. 1987; Yeh and Elsberry 1993a,b; Lin et al. 1999, 2005; Kuo et al. 2001; Huang and Lin 2008; Jian and Wu 2008; Y.-H. Huang et al. 2011; Lin and Savage 2011; Hsu et al. 2013, 2018; Tang and Chan, 2014, 2015, 2016; Wu et al. 2015; Huang et al. 2016a).

It has been generally recognized that influences upstream of the mountain range may be induced on the track within a critical distance from the CMR for westbound typhoons (e.g., Yeh and Elsberry 1993a,b; Y.-H. Huang et al. 2011; Wu et al. 2015; Tang and Chan 2016; Hsu et al. 2018). Consequently, westbound tropical cyclones tend to take a northward or southward track deflection as they approach the mountains at a distance of about the half-width scale of the mountain elongation (e.g., Wu et al. 2015; Huang et al. 2016a; Tang and Chan 2016).

For the CMR, the typical distance of track sensitivity is thus about 100–300 km as shown by a variety of idealized as well as realistic case simulations. Such large variations of upstream influence may be related to the size, intensity, translational speed, and direction of an approaching typhoon (e.g., Wu et al. 2015; Tang and Chan 2016; Hsu et al. 2018). These observational and modeling results show large variations in track deflection associated with different approaching typhoons. In general, a slower larger westbound tropical cyclone is associated with larger track deflection, due to the earlier interaction of the outer cyclonic flow that passes over and/or around the southern part of a mountain range to converge with the inner typhoon vortex to the south of the center (e.g., Yeh and Elsberry 1993a,b; Wu et al. 2015; Huang et al. 2016a).

Although northward track deflection tends to prevail for westbound TCs when tracks are to the north of the centerline of the mountain that is the latitude through the peak of the idealized mountain (e.g., Yeh and Elsberry 1993a), southward or northward deflection may be possible for TCs tracking close to the central mountain base (e.g., Wu et al. 2015; Huang et al. 2016a). Such deflection is found to rely on several nondimensional parameters (e.g., Lin et al. 2005; Huang and Lin 2008; Huang et al. 2016a), and southward deflection is preferred for smaller and weaker TCs tracking to the centerline of a wider mountain range, namely a small ratio (R/L_y) of the TC effective size (mostly represented by the radius of TC maximum wind speed R and the length scale L_y of the mountain elongation). Northerly flow can be enhanced to the west of the TC center and east of the mountain range as a result of channeling effects (Y.-H. Huang et al. 2011), which are more related to local flow enhancement near the surface as the flow shrinks ahead of the mountain range (e.g., Wu et al. 2015). Indeed, significant midtropospheric "channeling" also exists over the mountain range, which largely explains why such stronger asymmetric northerly flow can lead to southward tracks near landfall (e.g., Huang et al. 2016a). When the ratio (R/L_y) is rather small, the track of a westbound TC will be deflected to the south, regardless of the TC intensity and translational speed.

The track deflection in the above studies indeed is linked with complicated dynamics including effects of latent heating. To directly identify the contribution of diabatic heating to vortex motion, the potential vorticity (PV) tendency budget has been diagnosed. A dynamical framework of PV tendency diagnostics presented by Wu and Wang (2000) has been widely applied to investigate TC translation, and it is found that the translation is essentially dictated by PV advection and latent heating (e.g., Chan et al. 2002; Yu et al. 2007; Huang et al. 2016b;

Tang and Chan 2016; Hsu et al. 2013, 2018). Positive PV tendencies induced by asymmetric diabatic heating allow for a TC to shift to the region of upward heating gradient over an open ocean (Wu and Wang 2001). On the other hand, the geometric distributions of PV tendency can be significantly modified by topographic effects as a TC moves closer to a steep mountain. For example, a positive PV tendency may be enhanced by the Taiwan topography through asymmetric latent heating over the CMR, thus slowing down a departing typhoon (e.g., Hsu et al. 2013; Wang et al. 2012, 2013).

This study was motivated by a recent event of Typhoon Nesat (2017) that exhibited a large northward (rightward) track deflection as it approached the CMR. The typhoon began to deflect at a distance of about 300 km away from the ridgeline of the CMR and then exhibited a leftward deflection after landfall (see Fig. 3). In addition to the topographic influences of the CMR, the large track deflection of Nesat may also be influenced by a coexistent developing cyclone over the South China Sea (SCS) that moved toward the southern CMR as Nesat approached eastern Taiwan. We observed that several operational forecast models involved in daily prediction failed to capture the observed landfall of Nesat at northern Taiwan, mainly due to misprediction on the northward track deflection, for a forecast lead time only 2 days before the landfall.

To tackle the challenging issues of the track evolution associated with a TC in approximation to the steep CMR, regional models with nesting capability have been employed in the past. Alternatively, a global model, the Model for Prediction Across Scales (MPAS; Skamarock et al. 2012), with variable resolution of 60–15 km, where the higher 15 km resolution targeted on East Asia and offshore regions, has recently been applied to investigate the track evolution of typhoons over the western North Pacific (WNP) under the influence of large-scale flow variations (Huang et al. 2017). The enhanced resolution at the targeted region allows for a reasonable simulation of major structures of the approaching TC as regional models, while not suffering from the adverse impacts of lateral boundary conditions and abrupt change in nested domains of the latter (e.g., Hagos et al. 2013; Park et al. 2014). In this study, MPAS with a "double zooming" mesh using 60–15–3 km cell spacing is employed with the highest 3 km resolution centered over Taiwan to better resolve the topographic effects of the CMR as well as the convective systems associated with an approaching typhoon. We refer this high-resolution simulation to as "telescoped simulation" of TCs in the vicinity of the steep Taiwan topography. Simulations of global models with variable resolution of unstructured grids have been shown to give

performances comparable to use of uniform resolution, while greatly reducing the computational cost of the latter (e.g., Zarzycki et al. 2014; Sakaguchi et al. 2015). Grid refinement of global models at local regions improves both hurricane track and intensity forecasts compared to those without refinement (e.g., Zarzycki and Jablonowski 2015).

The paper is organized as follows. The model descriptions and configurations of both the global model MPAS and regional Weather Research and Forecasting (WRF) Model (Skamarock et al. 2008), together with their experimental setups are given in section 2. An overview of the evolution of Typhoon Nesat is presented in section 3. For reference, the simulated results using the regional model WRF for Nesat (2017) will be compared with MPAS simulations in section 4. The dynamics of Nesat's track evolution based on diagnostics of the PV tendency budget and wavenumber decompositions will also be included to highlight the contributions from different physical processes to typhoon movement (see the appendix). Sensitivity experiments aimed to identify the effects of the CMR and the cyclone over the SCS on the track deflection will be given in section 5. Influences of physical parameterizations on the track deflection of Nesat are investigated in this section. Finally, conclusions are given in section 6.
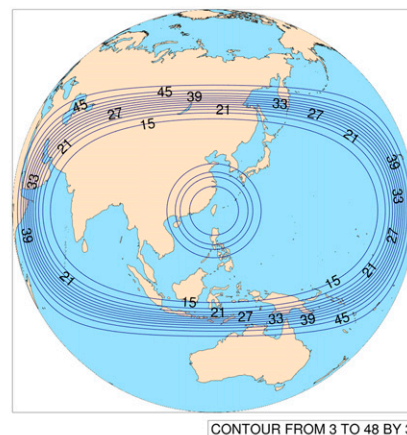
2. Models and experimental configurations

a. The MPAS model

The global model used in this study is MPAS, version 5.1, which is a nonhydrostatic global atmosphere model developed at NCAR (Skamarock et al. 2012). The unstructured centroidal Voronoi mesh allows variable resolution with smoothly varying mesh transitions. This alleviates many problems associated with the traditional mesh refinement strategies of one-way and two-way grid nesting employed in regional models, where the transitions are abrupt (Skamarock et al. 2012; Hagos et al. 2013; Park et al. 2014).

In this study, the 60–15 km variable resolution in Huang et al. (2017) is further extended to 60–15–3 km as shown in Fig. 1. The highest 3 km resolution region is centered over Taiwan and covers the major paths of many typhoons relative to the CMR. The maximum height of the CMR resolved by MPAS 3 km resolution is about 3600 m (see Fig. 3). With such variable-resolution, MPAS can provide commensurable capability of multiply nested regional models. Currently MPAS comes with two physics scheme suites, a mesoscale suite and a convective suite. For 3 km resolution used in this study, we employ the convective suite as described in Table 1.
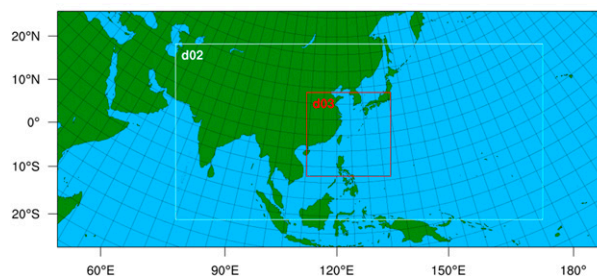

FIG. 1. (a) MPAS grids of 60–15–3 km variable resolution where the most inner zone is 3 km resolution (contours at an interval of 3 km), and (b) WRF nested grids at 45, 15, and 3 km resolution at domain 1, 2, and 3, respectively.

References for these physics schemes can be found in the technical note [Skamarock et al. (2008), available online at http://wrf-model.org]. The initial conditions were taken from the National Centers for Environmental Prediction (NCEP) Global Data Assimilation System (GDAS) Final Analysis Data ($0.25° \times 0.25°$), which have 31 vertical levels ranging from 1000 to 1 hPa and are updated every 6 h. During the model integration, the sea surface temperature is kept unchanged.

b. The WRF Model

We also utilized the Advanced Research version of the regional WRF Model for comparisons with the global MPAS model simulation for Nesat. The initial conditions and model physics used in the WRF simulation are identical to those for the MPAS simulation. The global model MPAS may offer the advantage of not being affected by the imposed lateral boundary conditions (e.g., Wu et al. 2005). While sharing nearly the same horizontal resolution, the WRF simulation employs nested domains with resolutions of 45, 15, and 3 km, respectively, as shown in Fig. 1b. The WRF-15 km domain is similar to the region embedded by the MPAS 15 km boundary, while the WRF 3 km domain

TABLE 1. Physics schemes and the numerical experiments conducted by MPAS. The physics schemes are listed for the control experiment CTL. Acronyms of the physics schemes: Grell–Freitas convective cumulus parameterization (Grell–Freitas), the new Tiedtke convective cumulus parameterization (New-Tiedtke), a cloud microphysics scheme with prognostic ice, snow, graupel processes, and rain number concentration (Thompson), the Noah land surface model (Noah), Mellor–Yamada–Nakanishi –Niino Level-3 PBL parameterization (MYNN), Yonsei University (YSU) planetary boundary layer parameterization, the Rapid Radiative Transfer Model for General Circulation Models (RRTMG) longwave and shortwave scheme, Xu–Randall cloud fraction parameterization (Xu–Randall), and WRF single-moment 6-class microphysics scheme (WSM6).

Parameterization	MPAS
Cumulus convection	Grell–Freitas
Cloud microphy"sics	Thompson
Land surface	Noah
Boundary layer	MYNN
Surface layer	MYNN
Radiation LW/SW	RRTMG
Cloud fraction for radiation	Xu–Randall

Experiment	Description
CTL	Initial field from NCEP FNL data with the above physical schemes
noT	As in CTL, but with the CMR reset to plain
noVT	As in CTL, but with removal of the initial low system over the SCS
WSM6	As in CTL, but using cloud microphysics scheme WSM6
NT	As in CTL, but using cumulus parameterization scheme New-Tiedtke
YSU	As in CTL, but using PBL scheme YSU with Monin–Obukhov surface layer

resembles that of the MPAS 3 km boundary. The initial and lateral boundary conditions for WRF are also from the NCEP GDAS Final Analysis Data. The main purpose of the model intercomparison is to realize the capability and reliability of the MPAS 3 km resolution in resolving the finescale convection and topographic effects.

3. Typhoon Nesat and experiments

a. Typhoon Nesat (2017)

Nesat originated east of the Philippines over the WNP and was categorized as Tropical Storm at 0600 UTC 27 July 2017 by the Japan Meteorological Agency (JMA). After 27 July, Nesat moved mainly west-northwestward, while gradually intensifying. On 29 July, Nesat reached its strongest state with the central sea level pressure (SLP)

of 960 hPa and maximum wind speed of $40\,m\,s^{-1}$. Nesat began to deflect northward near this time at a distance of about 300 km away from the ridgeline of the CMR. It later made landfall at northeastern Taiwan at 1200 UTC 29 July, and then turned somewhat leftward after passing over the northern CMR. Several operational models at weather forecast centers in East Asia and the United States predicted Nesat's landfall at southeastern Taiwan without the northward deflection or in central eastern Taiwan with much weaker deflection for a forecast lead time of only two days at 0000 UTC 28 July (see http://www.typhoon2000.ph).

b. Numerical experiments

In this study, several sensitivity experiments including the control experiment (CTL) are conducted and described in Table 1. For CTL, both MPAS and WRF have employed the same physics package for intercomparisons. Experiment noT that resets the CMR to a plain is conducted for exploring the topographical influence of the CMR on the typhoon track. The experiment noVT removes the initial cyclone over the SCS. A nonlinear balance equation is solved to obtain the initial field with the removed cyclone at a radius of 400 km by applying the default module of WRF (Davis and Low-Nam 2001). This SCS cyclone provides southwesterly conveying flow into the Taiwan area and is speculated to play an important role in the movement of Nesat near Taiwan.

4. Results

a. Simulations of Typhoons Soudelor (2015) and Megi (2016)

We first conduct experiments for intense Typhoon Soudelor (2015) and moderate Typhoon Megi (2016) to present the feasibility of MPAS-telescoped simulations crossing the resolution changes from 15 km to 3 km. The typhoon center in the track is defined as the minimum-wind speed location of the typhoon vortex averaged from the surface to about 8 km height above the surface. These two recent typhoons exhibit similarly tracks northwestward toward Taiwan but with smaller northward deflection compared to Nesat.

Figure 2a shows the simulated track of Soudelor for MPAS. MPAS captures the observed track up to 0000 UTC 6 August and after that a southward deviation leads to landfall at southeastern Taiwan rather than the observed near-central eastern Taiwan. Nevertheless, the 5 day track error of MPAS is still less than 150 km. For both central SLP and maximum near-surface wind, the MPAS solution exhibits similar variations in intensity as the observed (figures not shown).
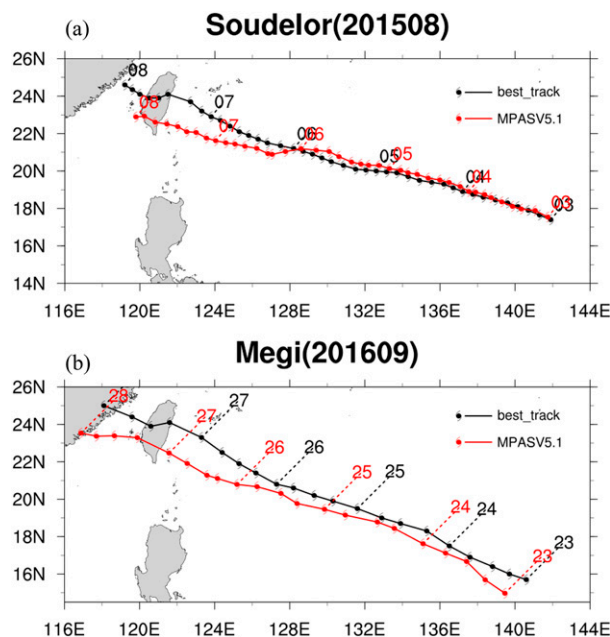
FIG. 2. (a) The observed best track (black) and simulated tracks by MPAS (red) for 5 day forecast of intense Typhoon Soudelor starting from 1200 UTC 3 Aug 2015, and (b) as in (a), but for moderate Typhoon Megi starting from 0000 UTC 23 Sep 2016.

For Typhoon Megi, MPAS also gives reasonably good track prediction for the first three days (23–26 July) consistent with the observed west-northwestward translation as shown in Fig. 2b. The larger track deviation near start-up is resulted from development of an initial weak cyclone without relocation to the best track position. After about 26 July, MPAS track begins to deviate with a southward bias. MPAS predicts a typhoon landfall at southeastern Taiwan, about 150 km southward of the observed landfall position. The 5 day track error of Megi from MPAS is also less than 150 km. For the intensity forecast, MPAS appears to capture the deepening of Megi as well.

b. Track and rainfall simulations of Nesat

The previous two cases also exhibit the models' difficulties in capturing the track deflection at early forecast lead times (e.g., 4 days before landfall). Therefore, the initialization time for Nesat is only 2 days before landfall, for a purpose of dynamic investigation of the observed track deflection. The simulated track and intensity of Nesat for both MPAS and WRF are compared in Fig. 3. Both MPAS and WRF predict consistently good tracks in the first day (28 July). Near 1800 UTC 28 July, Nesat appears to begin to deflect northward (or rightward of the upstream track). Both MPAS and WRF also predict the northward deflection at about 0000 UTC 29 July, but the WRF track
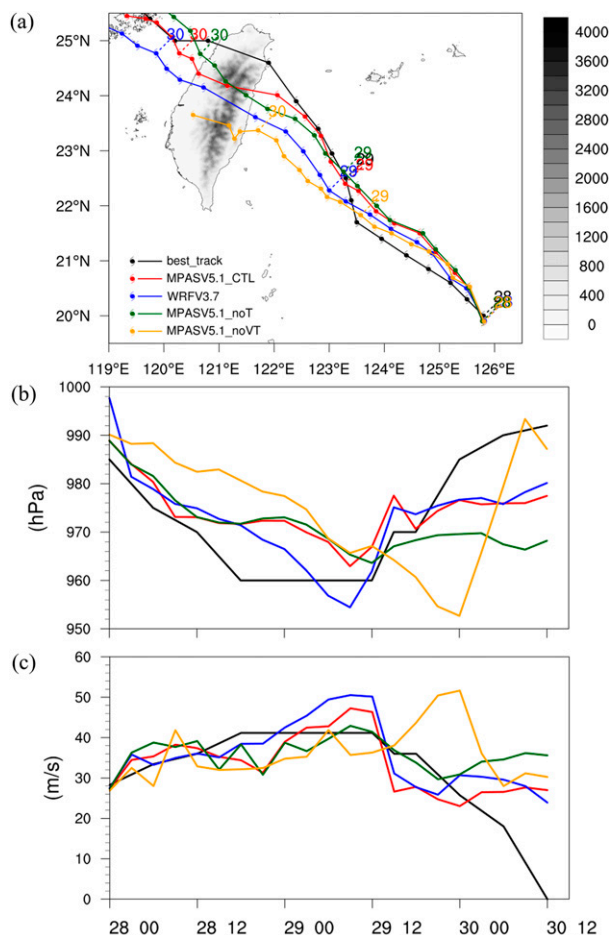

FIG. 3. (a) The observed best track (black) from JMA and simulated tracks of several experiments by MPAS and WRF (blue) for 60-h forecast of Typhoon Nesat starting from 0000 UTC 28 Jul 2017, (b) as in (a), but for central sea level pressure, and (c) as in (b), but for maximum wind speed at 10-m height. Taiwan topography (in m) resolved by MPAS 3 km resolution is overlapped by shaped gray color in (a).

is southward-biased with weaker deflection. MPAS obtains a more pronounced northward deflection in better agreement with the observed, but at a translation speed slightly slower than the best track speed (Fig. 3a). Consequently, the landfall position for MPAS is closer to the observed landfall at northeastern Taiwan, but still with a southward error of about 70 km, compared to about 120 km error for WRF. This southward track bias may be due to the fact that the intensity of the cyclone over the SCS is underpredicted by MPAS as Nesat is approaching the CMR. The impact of the cyclone over the SCS will be investigated later in section 5. Nevertheless, the general behaviors of the track evolution are reasonably simulated by MPAS. On the other hand, both MPAS and WRF capture the evolution of typhoon intensity well. WRF seems to slightly
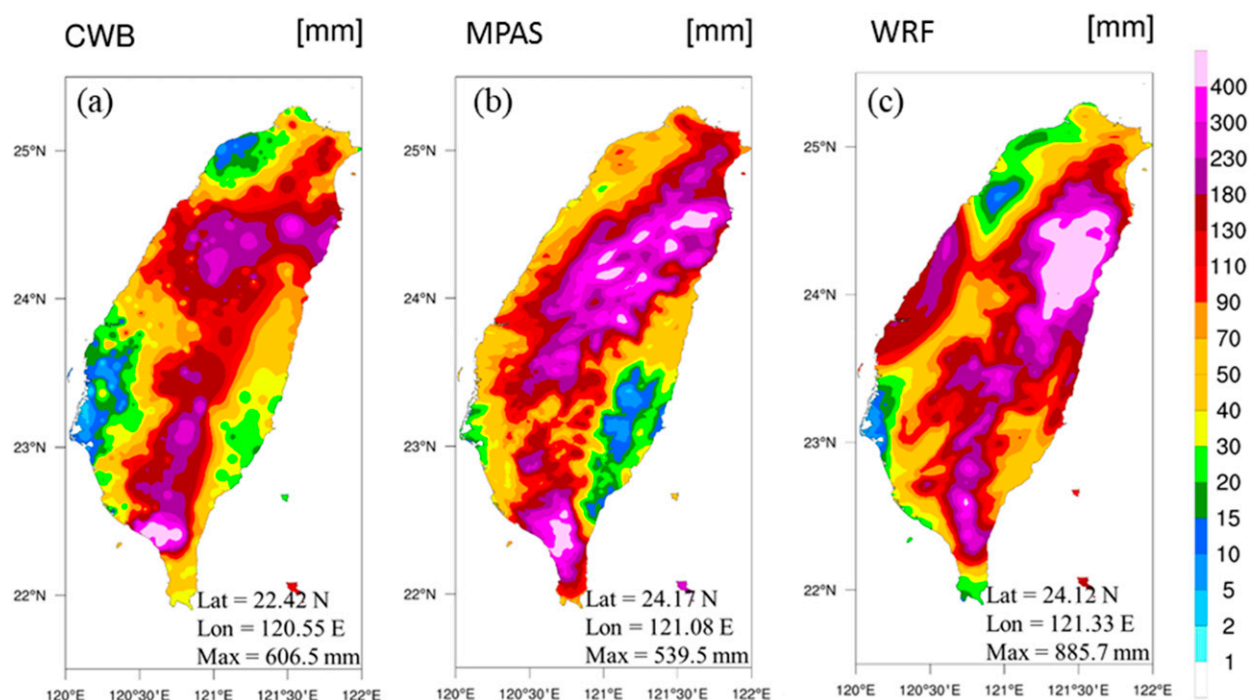
FIG. 4. The 48-h accumulated rainfall (shaped colors at units of mm with a reference bar to the right) (from 0000 UTC 28 Jul to 0000 UTC 30 Jul 2017) for (a) CWB observation, (b) MPAS simulation, and (c) WRF simulation.

overpredict the maximum intensity of central SLP and near-surface wind speed as compared to those from MPAS.

Figure 4 shows the 48 h accumulated rainfall from 0000 UTC 28 July to 0000 UTC 30 July for the CWB observations and the simulations of MPAS and WRF. Observed major rainfall occurs in the vicinity of northern Taiwan and along the southern slope of the CMR. The northern concentrated rainfall is primarily produced by the incoming upslope flow of the approaching typhoon before landfall, then followed by the southern major rainfall in response to the outer cyclonic flow of the typhoon near and after landfall (figures shown later). MPAS captures the distributions and intensities of two major rainfalls, but also produces too much rain over the central CMR, mainly due to the southward-biased track after landfall. We note that the maximum rainfall occurring near the southern end of the CMR is well simulated by MPAS, as benefited by the consistent track before landfall with similar observed northward deflection. In contrast, the WRF rainfall appears to be much larger with a maximum of 886 mm over the windward slope of northeastern Taiwan and farther southward extension than the observed and the MPAS rainfall, which is intimately related to its southward-biased track through the central CMR. Note that

both model performances are influenced by internal physical processes used in their simulations and the intercomparisons on only one case are not indicative of any surpass of the zoomed MPAS over nested WRF in this study.

c. The typhoon circulation, convection, and translation

Figure 5 shows the simulated horizontal wind and vertical velocity at 850 hPa near the commencement of deflection and landfall, respectively. Near the deflection of Nesat, a strong convergence zone is produced southeast of Taiwan consistent with intense upward motions (Fig. 5a), resulting from the outer cyclonic skirting flow of the typhoon passing over the southern CMR and the southwesterly flow originating from the developing cyclone over the SCS and nearby. Near landfall, the intense upward motions migrate to the near-coastal region of northeastern Taiwan (Fig. 5b). The upslope flow over the southern CMR becomes stronger, which explains why the rainfall maximum occurs near the southern tip of Taiwan near and after landfall (Fig. 4b). It should be noted that southwesterly flow may also be induced south of Taiwan when a westbound typhoon is departing from the CMR (e.g., Wang et al. 2013; Huang et al. 2016b). Thus, the presence of such intense southwesterly flow in fact
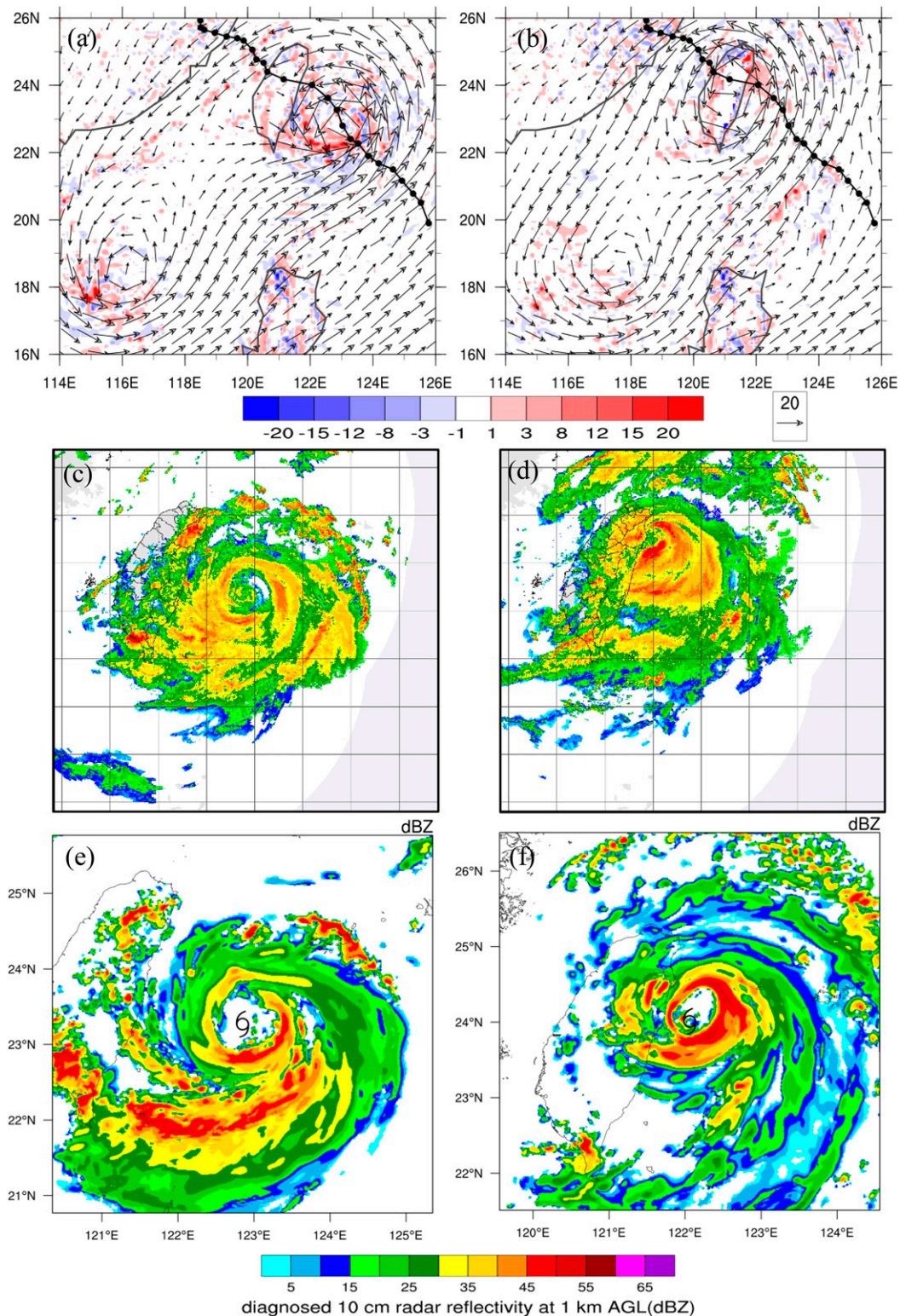
FIG. 5. (a) The simulated horizontal wind vectors (m s^{-1}) and vertical velocity (shaped colors, units: 10^{-1} m s^{-1} with a reference bar at the bottom) at 850 hPa at 0300 UTC 29 Jul 2017, and (b) in as (a), but at 1500 UTC 29 Jul 2017. (c) Radar reflectivity observation (color shaped at units of dBZ with a reference bar at the bottom) from CWB at 0600 UTC 29 Jul; (d) as in (c), but at 1100 UTC 29 Jul; (e) as in (c), but for the MPAS simulated radar reflectivity at 0600 UTC 29 Jul; and (f) as in (e), but at 1200 UTC 29 Jul. The simulated track (at an interval of 3 h) using MPAS is overlapped in (a) and (b).

pertains partially to the developing cyclone over the SCS, and partially to the environmental large-scale flow near these times.

The enhanced convergence southeast and east of the typhoon leads to intense convection as revealed by radar reflectivity in Figs. 5c and 5e, where both observations and simulations are in good agreement. As the typhoon moves closer to northern Taiwan and near landfall, the intense convection is produced mainly east of the typhoon center in the eyewall as simulated at 1200 UTC 29 July, well compared with the observed, but one hour later, since the simulated typhoon moves slightly slower (Figs. 5d,f). The observed strong convection further south of the eyewall and east of the southern tip of Taiwan, however, is almost absent in the simulation, which may be due to the fact that the typhoon begins to deviate farther to the south near this time (Fig. 3a).

The track deflection can be further illustrated by the close-up typhoon circulation and associated convective heating rate prior to and after deflection, as shown in Fig. 6. At 0300 UTC 29 July, Nesat began a northward deflection in response to the stronger southerly wind east of the typhoon center (Fig. 6a). Note that stronger upward motions (Fig. 6b) are mainly induced in the lower half annulus of the inner vortex where the inner flow and outer skirting flow converge and produce intense latent heating (Fig. 6c). As will be seen later, the southerly flow of the typhoon is also partially enhanced by the developing cyclone over the SCS. As the typhoon moves westward closer to the east coast, the high–wind speed region of the core has rotated counterclockwise to the northeast of the typhoon center (Fig. 6d), with intense upward motions and convective heating mainly tailing to the east (Figs. 6e,f). Near landfall, the high–wind speed zone rotates farther counterclockwise to the north of the inner vortex (Fig. 6g) to give stronger easterly wind and upward motions (Fig. 6h) as well as larger latent heating rate (Fig. 6i). The induced flow asymmetry dominated by the enhanced easterly wind at this time tends to drive the vortex more westward.
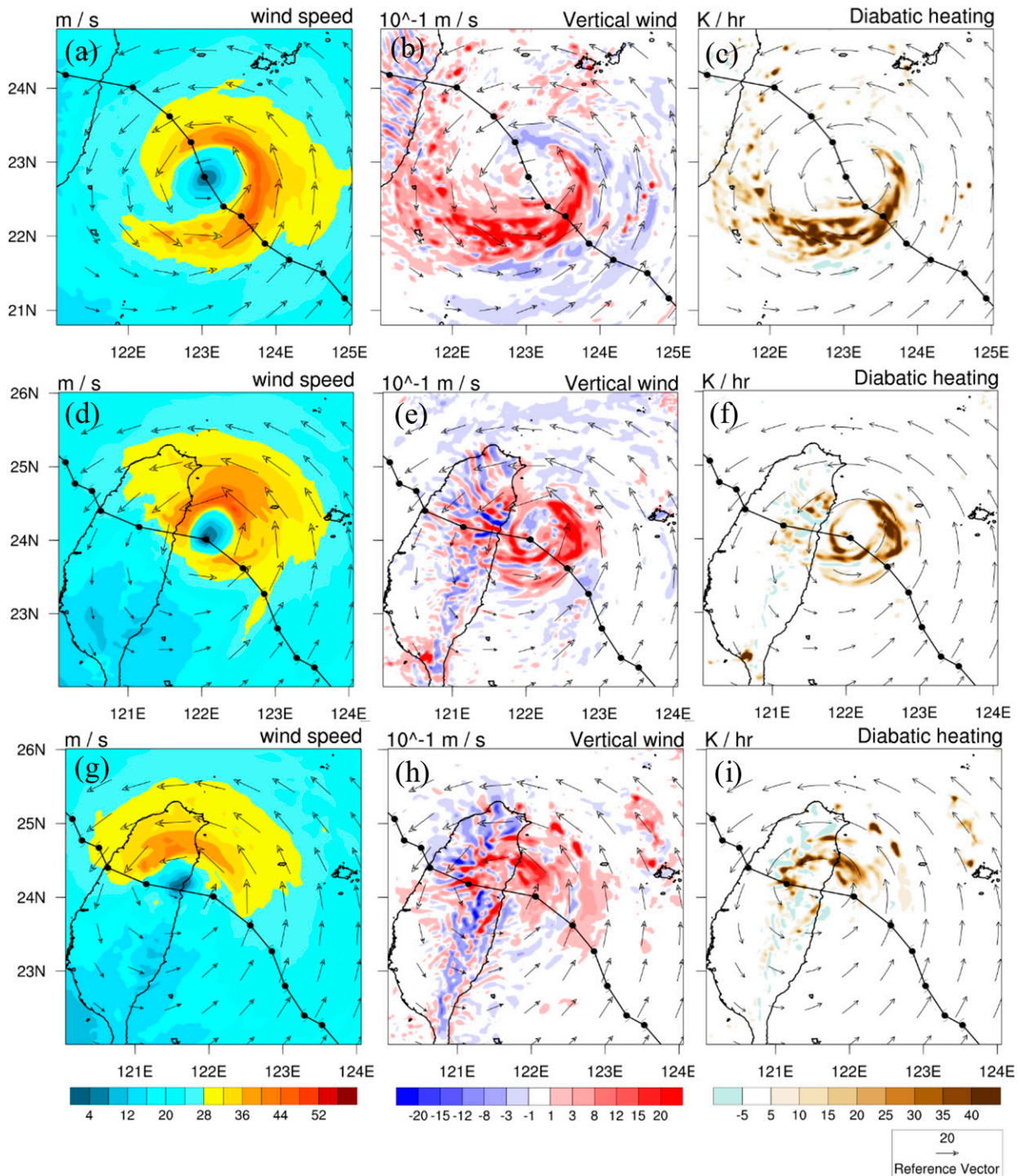
To further understand the track change, time evolution of the simulated typhoon translation speed and deep-layer mean steering flow are examined and compared to the observed translation speed in Fig. 7. The translation speed is calculated using the positions of the two typhoon centers 3 h before and after the analysis time. These three speeds in general exhibit similar trends, in particular near landfall (about 1200 UTC 29 July). For zonal translation, there are weak decelerations by 2100 UTC 28 July (early in the deflection) and then strong westward accelerations before 1500 UTC 29 July (prior to and near landfall) and then decelerations several hours after landfall (Fig. 7a). A large

increase in the northward velocity is evident from about 0000 UTC 29 July (Fig. 7b) when the inner vortex is associated with the high–wind speed region to the east of the center as seen in Fig. 6a. The northward translation quickly slows down after landfall with the high–wind speed region to the north of the center as seen in Fig. 6d, corresponding to a consistently more westward track (as to reduce the northward deflection). The combined translation of both directional speeds shows no significant change in the vortex translation speed except for some acceleration during landfall mainly due to the large increase in the westward zonal speed.

The large increase in translation speed during the northward deflection is clearly indicated by the presence of the high–wind speed region in the time evolution of both azimuthally averaged and radially averaged wind speeds. The azimuthally averaged wind speed exhibits a maximum core value (over $30 \, m \, s^{-1}$) lying at a radius of 50–100 km (Fig. 7c) during the phase of northward deflection (Fig. 7d). For a westbound typhoon the wind is stronger to the north (0°) starting from the initial time, but becomes weaker around the annulus and stronger to the south (180°) and later to the east (90°) as stronger northward deflection begins to take place around 0300 UTC 29 July. Again, the presence of the intense flow to the south and east is in accordance with the enhanced southwesterly flow from the developing cyclone over the SCS.

d. Diagnostics of PV tendency budget

The zoomed 3 km resolution reveals detailed vortex structures for diagnostics of the vortex dynamics regarding the track changes. The simulated PV and local PV tendency averaged over 1–8 km height at three stages of the deflection are analyzed in Fig. 8. The local PV tendency is computed using the PV outputs at 30 min after and before the analysis time. At 1500 UTC 28 July, the PV structure is rather symmetric (Fig. 8a) with scattered tiny PV tendencies in the vortex (Fig. 8b). In general, positive and negative PV tendencies are produced sporadically and more mixed to the south sector of the vortex. We may still identify some organized positive PV tendency at larger scales to the northwest of the center. At this time, the vortex is moving northwestward. At 0300 UTC 29 July, as the high–wind speed region migrates to the east and north of the vortex center (see Fig. 6a), intense PV is organized with a narrow band to the northeast of the center (Fig. 8c), which allows for larger positive PV tendency at the downstream side (i.e., to the north and west of the center) (Fig. 8d). Consequently, the vortex exerts the strongest northward deflection in response to the positive PV tendency. As the vortex moves

FIG. 6. The simulated results (shaped colors with a reference bar at the bottom) averaged in 1–8 km height at 0300 UTC 29 Jul 2017 for (a) horizontal wind speed(m s^{-1}), (b) vertical velocity (10^{-1} m s^{-1}), and (c) latent heating rate (K h^{-1}). (d)–(f) As in (a)–(c), respectively, but at 1200 UTC 29 Jul 2017. (g)–(i) As in (a)–(c), respectively, but at 1400 UTC 29 Jul 2017. The simulated track (at an interval of 3 h) and horizontal wind vector using MPAS are overlapped in each panel.
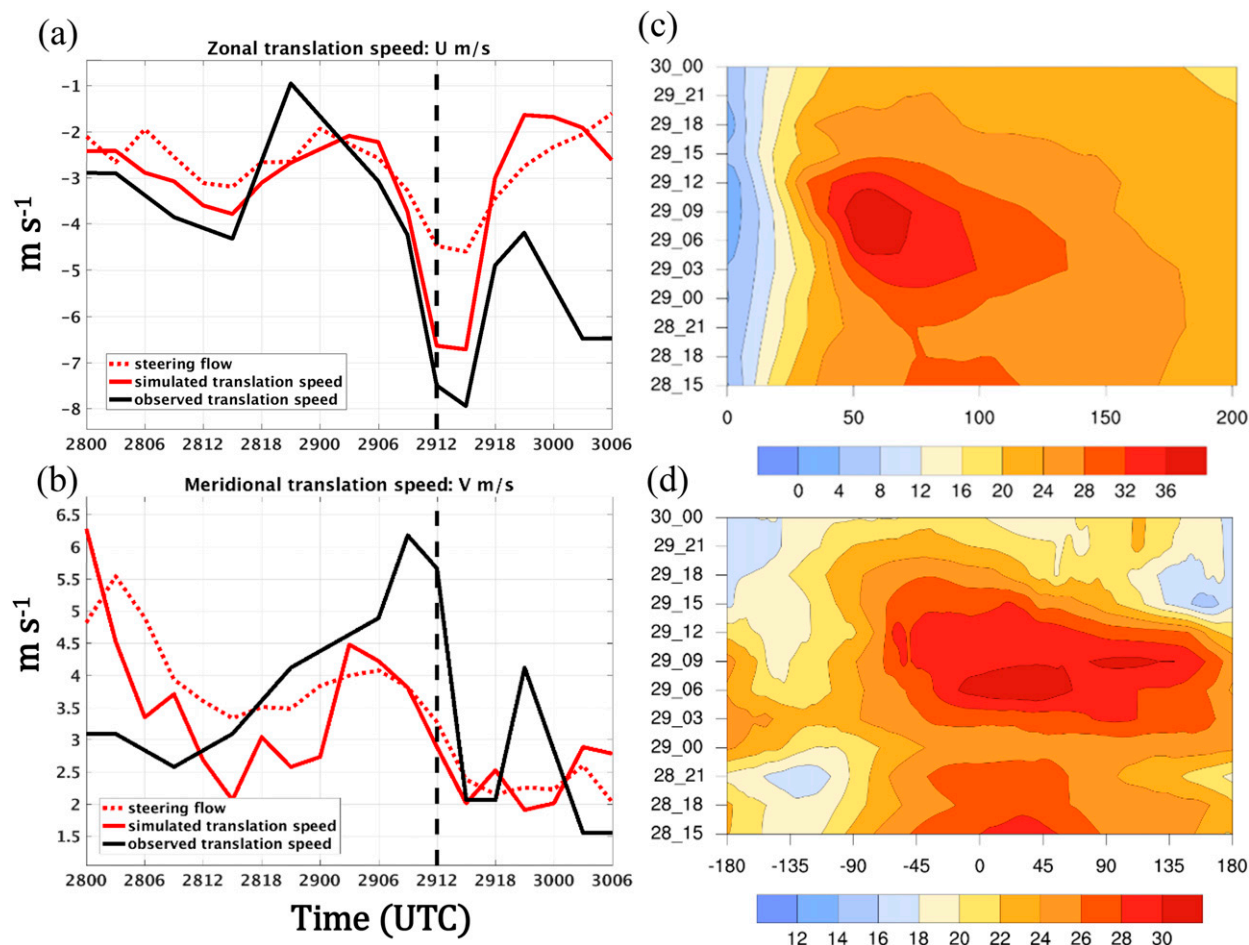
FIG. 7. (a) Time evolution of the simulated typhoon zonal translation speed (red), zonal speed component of steering flow (dashed), and the observed translation speed (black) in m s^{-1}, and (b) as in (a), but for the meridional speed, which is average in the radius of 400 km from the typhoon center and in 850–300 hPa height. The vertical dashed bar indicates the landfall time. (c) Time evolution of horizontal wind speed azimuthally averaged with respect to the typhoon radius (shaped colors, units: m s^{-1} with a reference bar at the bottom), and (d) as in (c), but for horizontal wind speed (m s^{-1}) radially averaged in 150 km from the typhoon center with respect to azimuthal angle (0° for north, 90° for east, −90° for west, and 180° for south).

northwestward and closer to the CMR at 0900 UTC 29 July, the intense PV band rotates counterclockwise (Fig. 8e) to produce larger positive PV tendency mainly to the north of the vortex center (Fig. 8f). Note that intense negative PV tendency in an arc-sharped zone is also produced southeast of the vortex center, which may help drive the vortex northwestward in response to the equivalent positive PV tendency to the northwest discussed later.

To identify the contributions to vortex translation from different dynamical processes, the wavenumber-1 (WN-1) PV tendency budget at the two deflection stages (0300 and 0900 UTC 29 July) is given in Fig. 9. Note that the budget uses averages within 30 min of the analysis time and over 1–8 km height. The net PV tendency is the sum of all the PV budget terms in

Fig. 9. The translation velocity regressed herein is also analyzed using the averaged budget. Northeastward translation at a speed of 2.87 m s^{-1} is induced by horizontal PV advection (Fig. 9b) when the most significant northward deflection is taking place. This effect is associated with the maximum PV to the northeast of the vortex center as seen in Fig. 8c. However, vertical PV advection will drive the vortex westward with a speed of 2.84 m s^{-1} (Fig. 9c). The induced translation by diabatic heating (latent heating) will be mainly eastward, but at a relatively smaller magnitude of 1.82 m s^{-1} (Fig. 9d) than those from both advection effects. Consequently, the effect of net PV tendency budget leads to weaker northeastward translation at a speed of 1.82 m s^{-1}, which, however, does not closely follow the WN-1 flow around the vortex toward the location of maximum PV
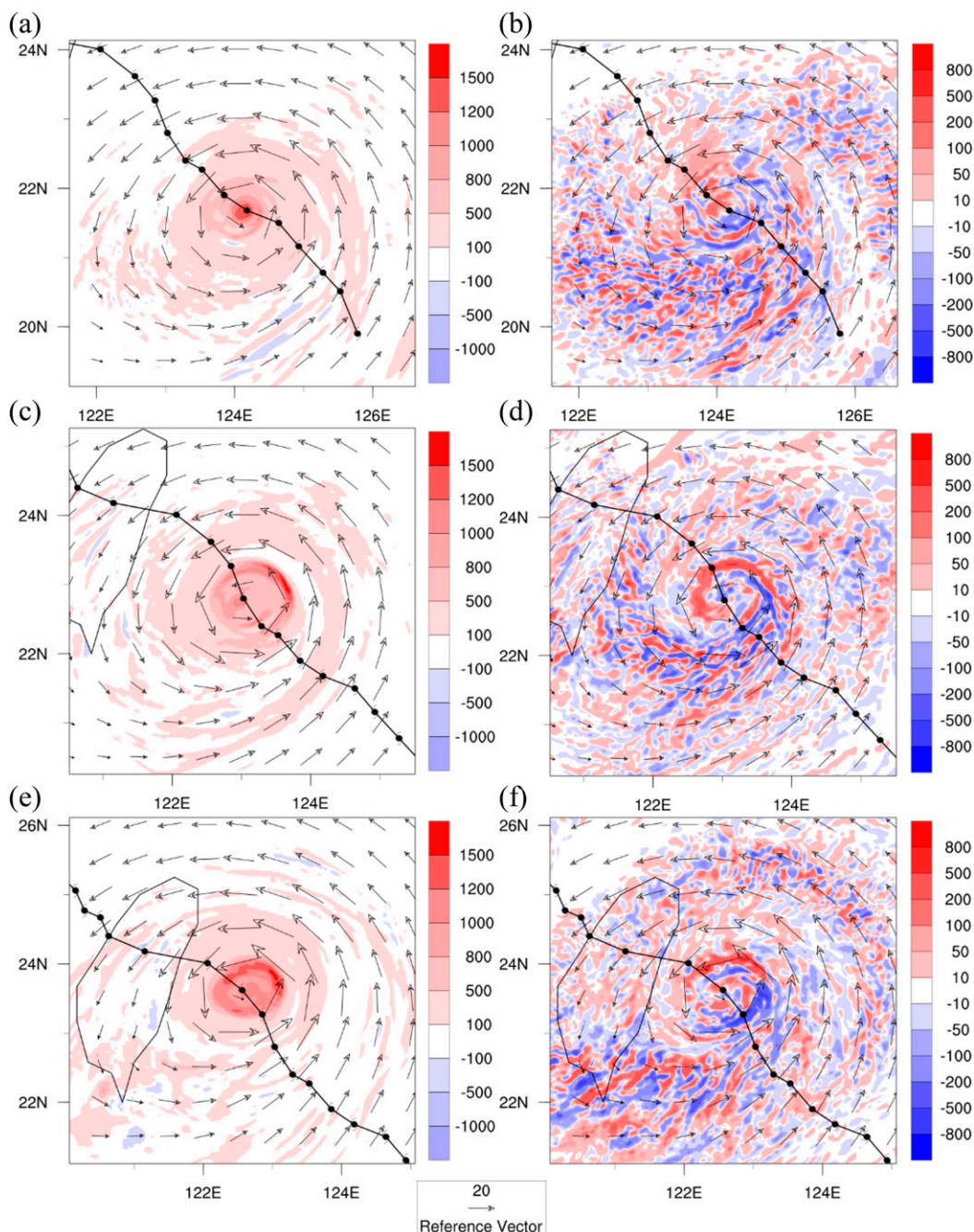
FIG. 8. (a) The simulated horizontal wind vector and PV (shaped colors with a reference bar to the right) averaged within 30 min of 1500 UTC 28 Jul 2017 and in 1–8 km height; (b) as in (a), but for net PV tendency; (c),(d) as in (a),(b), respectively, but at 0300 UTC 29 Jul 2017; (e),(f) as in (a),(b), respectively, but at 0900 UTC 29 Jul 2017. PV is in units of 10^{-2} PVU (1 PVU = 10^{-6} K kg^{-1} m^2 s^{-1}), and PV tendency is in units of 10^{-5} PVU s^{-1} (0.036 PVU h^{-1}). A reference wind vector (m s^{-1}) is given at the bottom right. The simulated track (at an interval of 3 h) using MPAS is overlapped in each panel.

tendency (Fig. 9a). We have further identified the difference between the regressed translation velocity and steering velocity and found that the high symmetric PV in the outer eyewall, as seen in Fig. 8c, indeed

dominates the regressed translation of the whole vortex. A maximum negative radial gradient of the symmetric PV is found near the outer eyewall about 75 km from the vortex center (figures not shown), which results in
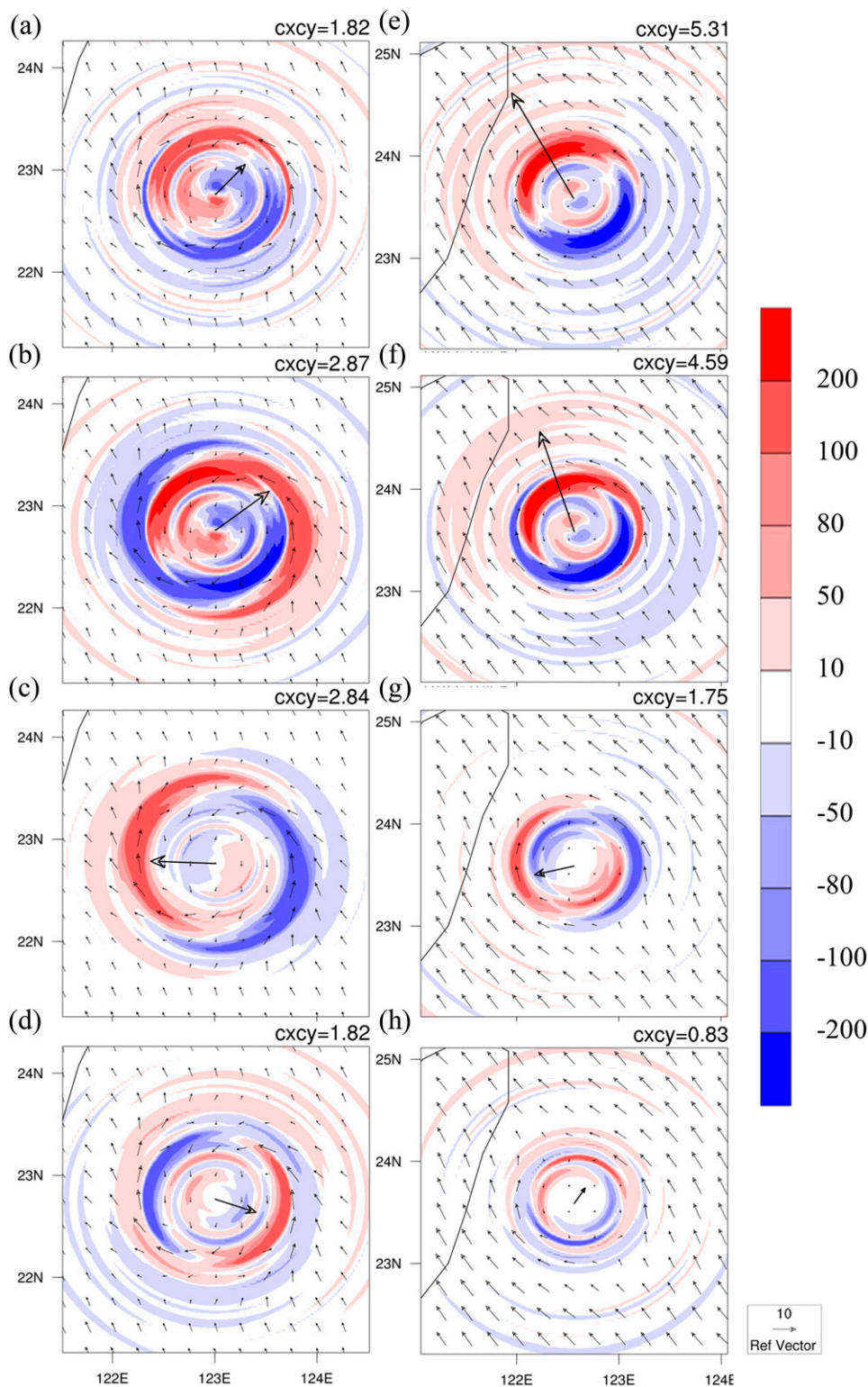
FIG. 9. The WN-1 horizontal flow and PV tendency budget (shaped colors with a reference bar to the right) averaged in 1–8 km height at 0300 UTC 29 Jul 2017, contributed by (a) net PV budget, (b) horizontal advection, (c) vertical advection, and (d) diabatic heating in PV tendency. (e)–(h) As in (a)–(d), respectively, but at 0900 UTC 29 Jul 2017. PV tendency is in units of 10^{-5} PVU s^{-1}. The number at the top of each panel indicates the magnitude of the translation speed corresponding to the vector at the typhoon enter. A reference wind vector (m s^{-1}) is given in the lower right for WN-1 flow component.
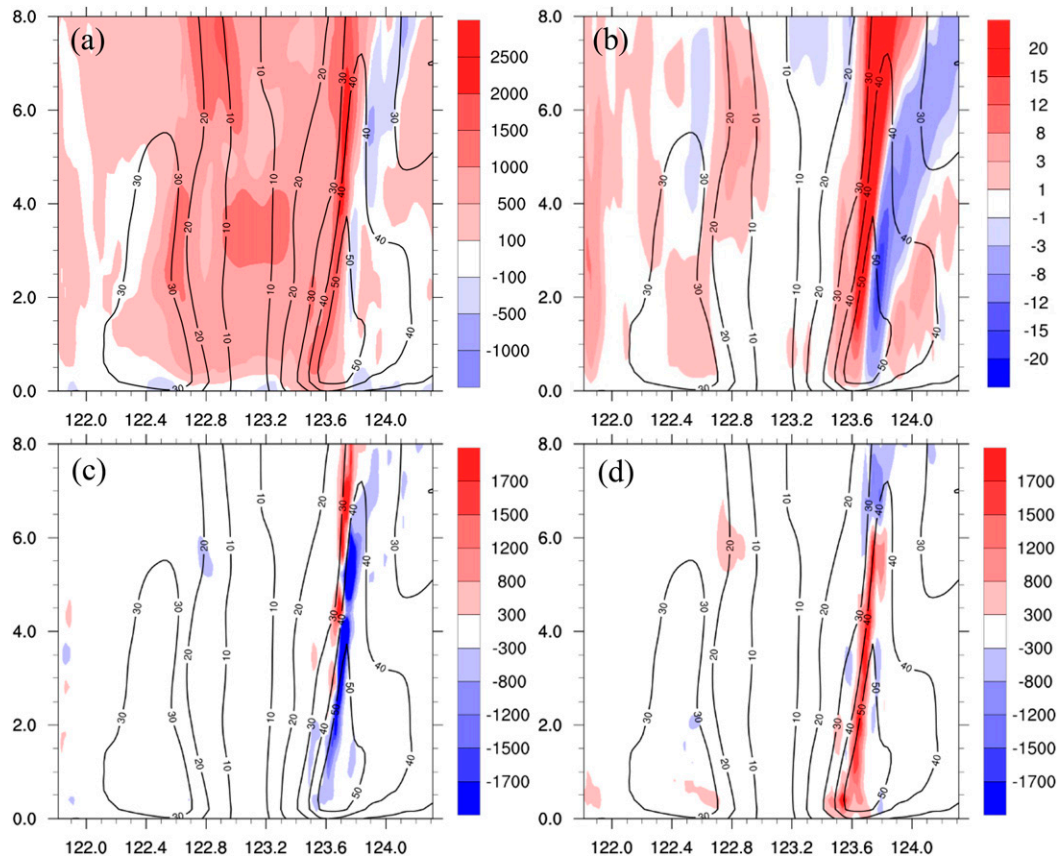
FIG. 10. The simulated results (shaped colors with a reference bar to the right) at zonal (longitude in degrees) and vertical (height in km) cross section through the vortex center averaged within 30 min of 0300 UTC 29 Jul 2017. (a) PV (10^{-5} PVU), (b) vertical velocity (10^{-1} m s^{-1}), (c) PV vertical advection, and (d) effects of differential latent heating. PV tendency budget is at units of 10^{-5} PVU s^{-1} (0.036 PVU h^{-1}). In all panels, contours of horizontal wind speed (m s^{-1}) at an interval of 10 m s^{-1} are overlapped.

mostly strong negative correlation with asymmetric net WN-1 PV tendency (Fig. 9a) and thus northeastward translation according to (A2) in the appendix. This is consistent with Wu and Wang (2000) that the regression method for a more asymmetric vortex may give a larger deviation from the actual vortex movement.

Horizontal PV advection tends to dominate the vortex translation at a speed of 4.54 m s^{-1} at 0900 UTC 29 July (Fig. 9f) when the vortex turns northwestward closer to the CMR (Fig. 9e). The large negative net PV tendency to the southeast of the vortex center (Fig. 8f) is mainly contributed by negative horizontal PV advection, which would equivalently induce positive WN-1 PV tendency to the northwest of the vortex center as seen in Fig. 9e. PV vertical advection continues to contribute to the westward translation speed but at a reduced magnitude of 1.75 m s^{-1} (Fig. 9g). The effects of diabatic heating now become much weaker (Fig. 9h), which may be related to the more symmetric PV structure as seen in Fig. 8e. The combined net

effect is to induce a large northwestward translation velocity which follows the environmental WN-1 flow quite well and points to the location of maximum PV tendency.

To further understand the vertical variations of the PV dynamics during the deflection, the simulated results in the zonal-vertical cross section through the vortex center are shown in Fig. 10. The eyewall is much stronger in the eastern sector in the troposphere than in the western sector in terms of both PV and vertical motions (Figs. 10a,b). Negative vertical PV advection is significant below 6 km height in the eastern sector, while it is very weak in the western sector (Fig. 10c). The PV intensity increases with height in the troposphere with upward motions in the eastern sector, allowing for negative PV transport below 6 km height. This may explain why the 1–8 km average of vertical PV advection exhibits negative effects at the eastern sector in Fig. 9c. This large negative contribution in turn will accompany the commensurate WN-1 positive
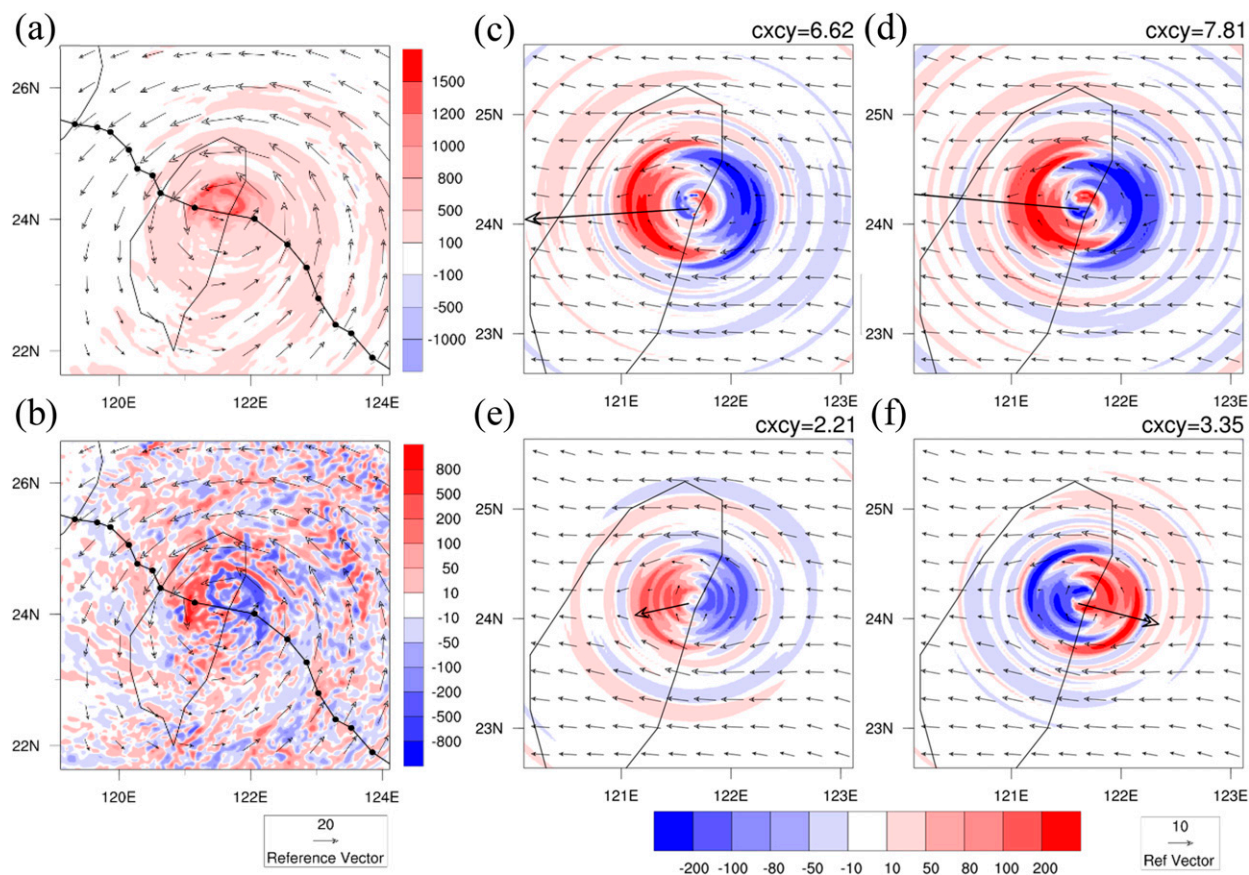
FIG. 11. (a) The simulated horizontal wind vector (m s^{-1}) and PV (shaped colors at units of 10^{-2} PVU with a reference bar to the right), both averaged within 30 min of 1400 UTC 29 Jul 2017 and in 3–8 km height, (b) as in (a), but for PV tendency, (c) net PV tendency budget, and contributions from (d) horizontal advection, (e) vertical advection, and (f) differential diabatic heating. In (c)–(f), shaped colors are at units of 10^{-5} PVU s^{-1} with a reference bar at the bottom. The simulated track at an interval of 3 h using MPAS is overlapped in (a) and (b) and the vector information in (c)–(f) is defined as the same in Fig. 10. The arrow of the translation vector is out of frame in (d).

counterpart that tends to drive the vortex westward. With the intense upward motions in the eastern sector, large positive contribution from differential latent heating is present below 6 km height, which supports the regressed translation roughly eastward in Fig. 9d when averaged in 1–8 km height.

As the vortex is making landfall at northeastern Taiwan near 1400 UTC 29 July, the vortex translation becomes more westward. At this time, the PV tendency budget is averaged in 3–8 km height since only a very small portion of the CMR exceeds 3 km height. Major positive PV is produced in the northern sector of the inner vortex core and over the northern CMR (Fig. 11a), which is in association with negative PV tendency in the eastern sector of the eyewall and positive PV tendency over the northern CMR (Fig. 11b). The large positive PV generation is associated with east-westward distribution in the net WN-1 PV tendency as seen in Fig. 11c, which mainly results from the dominant WN-1

horizontal PV advection in response to the cyclonic transport of positive PV, leading to large westward translation at a speed of 7.81 m s^{-1} in consistence with the actual TC movement (Fig. 11d). Positive WN-1 vertical PV advection now supports weaker and mainly westward translation at a speed of 2.21 m s^{-1}, which may be also related to the negative counterpart to the east of the vortex center (Fig. 11e). At this time, moderate translation at a speed of 3.35 m s^{-1} induced by diabatic heating mainly points to the east, again attributable to the negative contribution to the west of the vortex center (Fig. 11f). It is interesting to observe the retarding effect of differential latent heating as most of intense rainfall is being produced over the northeastern slope of the CMR at this time (see Fig. 4b).

Figure 12 shows the simulated results in the zonal-vertical cross section through the vortex center at the landfall time of 1400 UTC 29 July. As can be seen, the eastern sector of the eyewall remains roughly
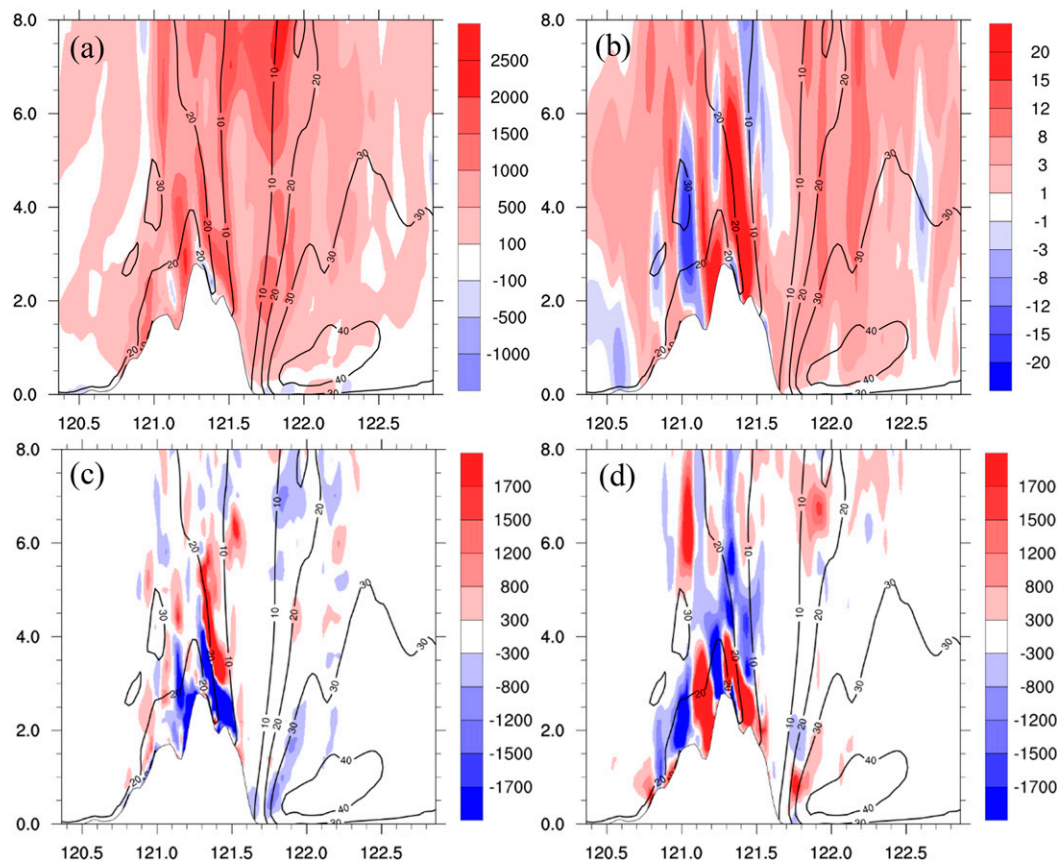
FIG. 12. As in Fig. 10, but at 1400 UTC 29 Jul 2017.

preserved, while the western sector over the CMR has been considerably destructed. Larger PV is mainly produced below 4–5 km height over the CMR and above 6 km height near the vortex center (Fig. 12a). Note that the PV intensity indeed is reduced near the surface of the CMR. The upwind side of the CMR is accompanied by strong upward motions up to 8 km height (Fig. 12b). Consequently, vertical PV advection becomes negative at lower levels and positive at higher levels below 7 km over the upward slopes of the CMR (Fig. 12c). Over the eastern sector, most of vertical PV advection is negative below 8 km height. Thus, as shown in Fig. 11, the effects of vertical PV advection averaged over 3–8 km height exhibit positive and negative contributions to the PV tendency in the western and eastern sectors, respectively. Because of the vertical cancelation of the effects in the western sector, contributions from vertical PV advection are not as large as from horizontal PV advection. Differential diabatic heating shows large positive contributions to the PV tendency below 3–4 km height over the CMR slopes above which the contribution becomes negative up to 8 km height. The presence of the

negative contribution from differential latent heating indicates that the heating indeed is stronger at these lower levels. This is consistent with the strongest upward motion (thus heating rate) near 4 km height (see Fig. 12b). The results may highlight the fact that the eastward retardation by the latent heating effects is due to its negative vertical differential over the CMR slopes. The induced large positive contribution to the east of the vortex center, as seen in Fig. 11f, is just the corresponding counterpart of the negative effects physically produced over the CMR slopes.

5. Discussion

We will discuss other interesting and important factors contributing to the track changes in this section. In this regard, we have identified the sensitivities to model physics schemes, the effects of the CMR and the cyclone over the SCS.

a. Influences of physical parameterization

Several sensitivity experiments have been conducted to explore the influences of physical parameterizations on
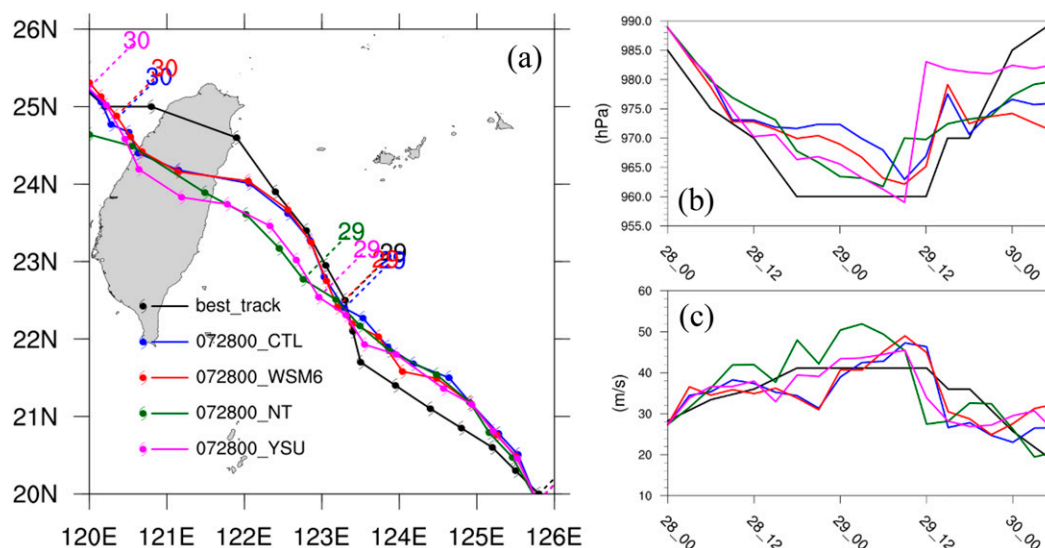
FIG. 13. As in Fig. 3, but for CTL (blue) and several physics sensitivity experiments: WSM6 (red), NT (green), and YSU (purple). The observed best track results are also plotted in black.

the typhoon evolution within the 3 km resolution region. These experiments help understand the predictability of the track deflection as the evolving typhoon size and structure are influenced by internal physical processes. Figure 13 shows the track and intensity evolution of the simulated Nesat in the physics-sensitivity experiments targeted for cloud microphysics (WSM6 scheme), cumulus parameterization (new Tiedtke scheme, NT) and PBL parameterization (YSU scheme). These schemes not only have different influences on track evolution but also on intensity. Both CTL (with the Thompson double-moment scheme) and WSM6 (single-moment scheme) obtain almost identical tracks showing consistent northward deflection (Fig. 13a), but with slightly stronger intensity for WSM6 in terms of central SLP (Fig. 13b). Northward track deflection is considerably reduced after 29 July for both NT and YSU, even using the same cloud microphysics as CTL. It is interesting to observe that the track deviations among the experiments begin to amplify as the deflection is taking place. However, we do not find that these four schemes exhibit large differences in TC intensity, except for the overpredicted stronger winds prior to landfall from NT and the underpredicted central SLP near and during landfall from YSU. Both NT and YSU tracks are comparable to the operational HWRF forecast at the same lead time (see http://www.emc.ncep.noaa.gov/gc_wmb/vxt/HWRF). It is interesting to find that physical parameterizations for cumulus and PBL effects could be more influential in the track evolution of the intensified typhoon closer to the CMR than at earlier stages over the open ocean. Further

examination of these physical parameterization schemes on variable-resolution grids is not within the scope of this study.

b. Terrain effects on track deflection

For direct comparisons, we also conducted several experiments where some model conditions are reset as described in Table 1. The time evolution of the simulated tracks and intensities for these experiments have been shown in Fig. 3. As the CMR height is flattened in noT, the northward deflection is reduced as well, but not significantly. Compared to CTL, the typhoon intensity near landfall is less modified for noT, but the aforementioned high–wind speed region is weaker and less extended into the east sector of the vortex (figures not shown).

We also calculate the simulated PV and WN-1 PV tendency budget (averaged in 1–8 km height) for noT at 0900 UTC 29 July (about 5 h before landfall). The intense PV annulus in the inner vortex is more symmetric with larger negative PV tendency to the southeast of the center (figures not shown). The west-northwestward translation at a speed of 2.32 m s^{-1} indicated by the net WN-1 PV tendency is in good agreement with the surrounding steering flow and with the actual vortex movement which is largely driven by the westward translation induced by the dominant horizontal PV advection and the weaker differential latent heating. At this time, vertical PV advection contributes a comparable northeastward translation speed of 2.1 m s^{-1}. We find that the PV tendency budget at 0300 UTC 29 July for noT is also more dominated by horizontal PV advection as in CTL

(see Fig. 9). Differential latent heating in the absence of the full CMR contributes a PV tendency at smaller magnitudes with no persistent translational direction with time. Vertical PV advection tends to retard the westward translation of the vortex at this time, which is contrary to the acceleration in CTL. Contributions from vertical PV advection and the effects of differential latent heating appear to counteract each other to some extent, regardless of the presence of the CMR.

c. Impact of the cyclone over the South China Sea

It has been observed that a low pressure system is also developing with time over the South China Sea (SCS) as a westbound typhoon is approaching Taiwan. For example, the developing Goni cyclone near Hong Kong over the SCS has been found to contribute to the intensification of the southwesterly flow southwest of Taiwan and the extreme rainfall over southern Taiwan as Typhoon Morakot (2009) is near and after landfall at eastern Taiwan (e.g., C.-Y. Huang et al. 2011). There is no indication that Morakot's movement at later stages was influenced by the developing Goni. Binary interaction between two adjacent typhoons in the vicinity of Taiwan causing their track changes has been illustrated by Tropical Storm Bopha and Supertyphoon Saomai in 2000 (e.g., Wu et al. 2003), Typhoons Fengshen and Fungwong in 2002 (e.g., Yang et al. 2008), and Typhoon Tembin and Supertyphoon Bolaven in 2012 (e.g., Liu et al. 2015). However, none of the above cases was associated with a major stronger typhoon that made landfall at Taiwan.

The simulated intensity of the cyclone is underpredicted after the northward deflection of Nesat begins to emerge at 1200 UTC 28 July in CTL (see Figs. 3b,c). The model fails to predict the increasing intensity of this cyclonic system, which could lead to a southward-biased track of Nesat near and after landfall. In Experiment noVT, removal of the initial cyclone southwest of Taiwan has affected the track deflection of Nesat and produced a slowdown in the vicinity of Taiwan as seen in Fig. 14. Note that a northward track deflection but closer to landfall followed by a southward deflection after landfall is prominent for noVT, which is similar to idealized simulations (Huang et al. 2016a). Because of the slower-crossing track through central Taiwan, the typhoon intensity has significantly weakened after landfall (see the green line in Figs. 3b,c). Figure 14 also shows the simulated circulations (averaged in 1–8 km height) at 0300 UTC 29 July for CTL and noVT. The simulated cyclone over the SCS at the simulation end moves northeastward to offshore of eastern Taiwan with a lagging track (Fig. 14a), while the observed TC is offshore west of the southern tip of Taiwan (Fig. 15a).
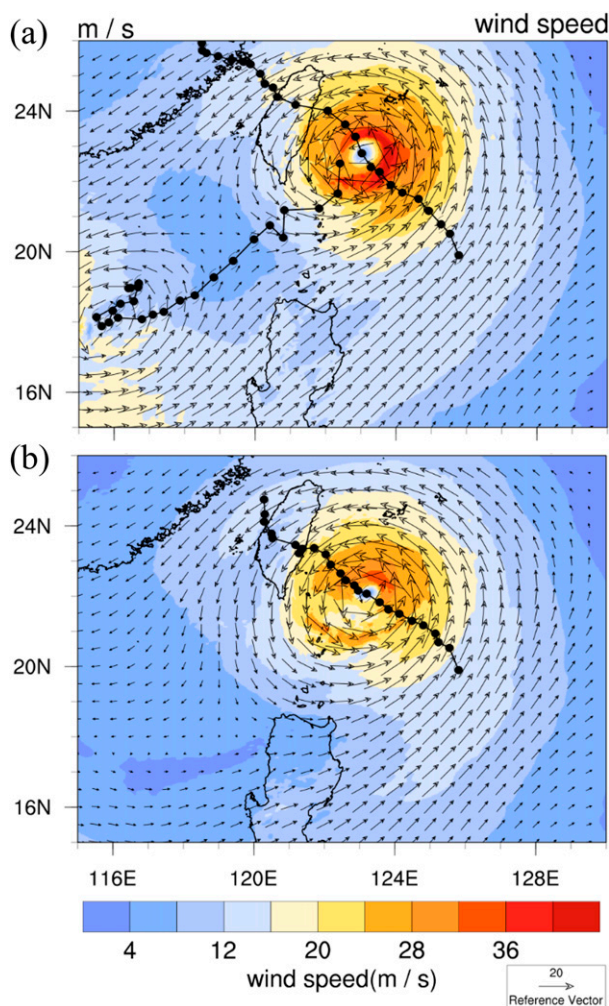

FIG. 14. The simulated horizontal wind vector (m s^{-1}) averaged in 1–8 km height at 0300 UTC 29 Jul 2017 for experiments (a) CTL and (b) noVT. Shaded colors represent horizontal wind speed (m s^{-1}) with a reference bar at the bottom. The simulated tracks of the Nesat typhoon and the cyclone over the South China Sea starting from 0000 UTC 28 Jul 2017 for 72 h are overlapped by the black solid cycles at an interval of 3 h.

In addition, the simulated intensity of the cyclone is underpredicted by 3–10 hPa after the northward deflection of Nesat begins to emerge at 1200 UTC 28 July in CTL (figures not shown). As the initial cyclone has been removed in noVT, the southwesterly flow becomes much weaker west of the northern Philippines. Without a conveying belt of enhanced southwesterly momentum into Nesat, the stronger wind to the south and east of the typhoon center is suppressed (Fig. 14b). Consequently, Nesat is driven northwestward without a large northward (or rightward) deflection prior to landfall mainly following the more intense easterly flow to the north of the typhoon center. The observed SCS cyclone moves northeastward toward southern Taiwan
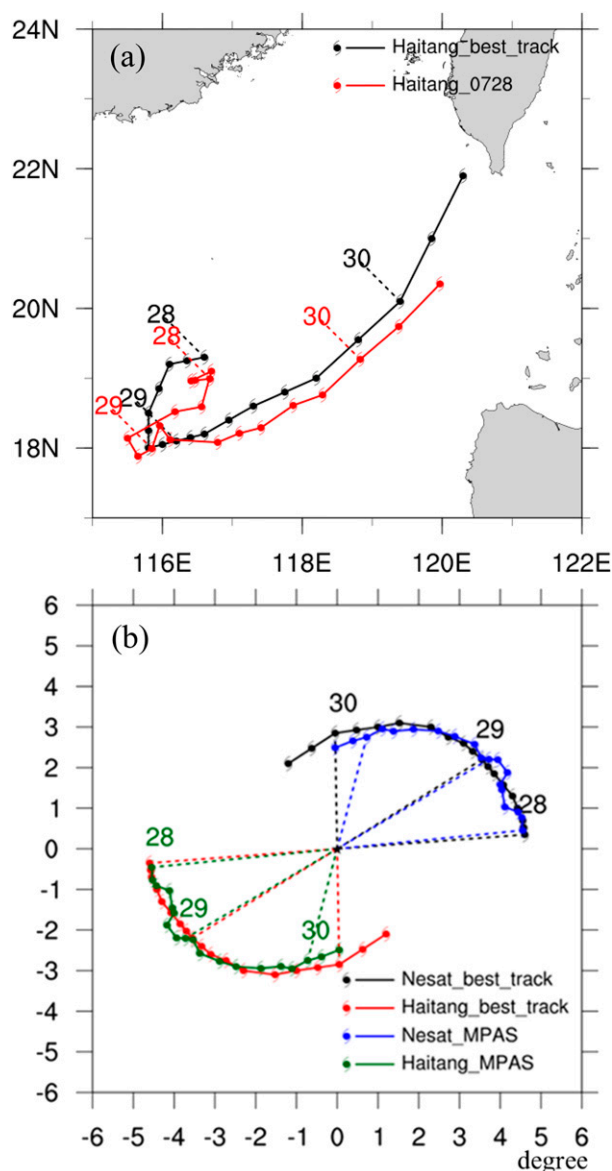
FIG. 15. (a) The simulated track (red) and the best track (black) of Tropical Storm Haitang at an interval of 3 h shown from 0000 UTC 28 Jul to 0600 UTC 30 Jul 2017. (b) Relative positions of the centers of Nesat and Haitang in an interval of 3 h for the best track and MPAS simulations in the east–west and north–south coordinates (in degrees).

after 0300 UTC 29 July, with increasing intensity of central SLP (figures not shown). The model fails to predict the increasing intensity of this cyclonic system at later times, which could lead to a southward-biased track of Nesat prior to and after landfall.

Comparing CTL and noT simulations, the SCS cyclone appears to have stronger impacts on later Nesat's track than the CMR. Note that the separation of the center positions of the cyclone and Nesat is about

1000 km, which is still within the critical distance of about 1400 km for the Fujiwhara effect to take place (Fujiwhara 1921). To examine any possible Fujiwhara effect between the two cyclones, Fig. 15 shows the cyclone track and the relative positions of the centers of Nesat and the cyclone (once developed into a tropical storm named as Haitang). As seen, the two cyclones are taking a counterclockwise rotation around each other in both simulations and observations. MPAS simulations capture the relative positions of the two cyclones quite well prior to their approaching to the CMR. Note that the binary interaction between the two cyclonic systems at later times after Nesat's landfall still maintains a well-defined counterclockwise rotation in spite of the interference of the CMR.

6. Conclusions

Typhoon Nesat (2017) headed straight west-northwestward toward Taiwan but experienced a large northward track deflection about 300 km away and then a leftward deflection after landfall at northeastern Taiwan. The global model MPAS, employing multi-resolution mesh of 60–15–3 km, is applied to investigate the track changes and the underlying mechanisms. By double zooming into the targeted region covering the typhoon path, the global model simulation is capable of explicitly simulating small-scale convection embedded in the typhoon and simulating the detailed topographical effects of the CMR in Taiwan. The variable-resolution simulation of MPAS compares better with the observed northward deflection of Nesat (2017) than the regional model simulation of WRF using comparable nested grids. The comparison illustrates the feasibility and reliability of telescoped simulation using the global variable-resolution model.

The track changes of Nesat are explained by WN-1 decompositions of PV tendency budget since the vortex movement is dominated by the WN-1 PV tendency (e.g., Wu and Wang 2000; Hsu et al. 2013). The northward track deflection is mainly in response to the WN-1 horizontal PV advection as the southerly flow east of the typhoon center is enhanced by convergence with the outer cyclonic typhoon flow over and around the CMR and with the large-scale southwesterly southwest of Taiwan. Upward motions and PV in the troposphere thus are much larger to the east of the vortex center than to the west, resulting in westward translation (thus leftward deflection) induced by negative WN-1 vertical PV advection but eastward translation by positive WN-1 vertical differential heating to the east of the vortex center. When larger upward motions and PV are produced at lower levels over the northern CMR near landfall, the vortex translation becomes westward because

horizontal PV advection dominates. The vortex translation is also somewhat modified by the other two processes. Vertical PV advection to the west of the vortex center becomes positive and contributes a smaller westward translation, while the associated vertical differential heating becomes negative to retard the westward translation.

It is not surprising that the simulated track deflection of Nesat for MPAS is somewhat dependent on the physical parameterizations. Use of single-moment (WSM6) instead of double-moment cloud microphysics produces almost identical tracks and deflections. However, use of the YSU PBL parameterization or New-Tiedtke cumulus parameterization results in considerably reduced deflection near landfall (comparable to the WRF simulation), but still with similar tracks before the deflection takes place. The simulated typhoon intensities in general show similar trends with time, except that YSU produces much weaker maximum wind speeds of the typhoon near and after landfall. Thus, it is believed that capturing the track deflection is more physics-dependent rather than dynamics-dependent as the tracks with varying physics start to diverge only after the deflection takes place.

Sensitivity experiments indicate that flattening the CMR only partially reduces the track deflection of Nesat, while the elimination of the initial cyclone over the SCS deactivates the Fujiwhara effect and leads to a southward-biased track with much weaker deflection prior to landfall. The binary interaction between Nesat and the SCS cyclone still maintains a counterclockwise rotation of each other even when both are appreciably affected by the CMR. The increasing influence of the approaching cyclone explains why the track deflection takes place at a relatively larger upstream distance (about 300 km) than regular conditions (100–150 km).

The feasibility and reliability of the MPAS-telescoped simulations targeted on the region of the typhoon path are presented in this study, and the diagnostics of PV tendency budget and the sensitivity experiments help explain the underlying mechanisms of the track deflection associated with Nesat in approximation to Taiwan. Although model uncertainties may be better realized from ensemble simulations with perturbed initial conditions and physics-induced tendencies, the observed large track deflection of Nesat can be realized in this study without resort to large ensembles. However, understanding of model uncertainties from ensemble spreads may help identify a wide spectrum of predictability for the Nesat's track with or without appreciable deflection.

APPENDIX

Formulations of PV Tendency Budget and Regressed Vortex Translation

To further understand dynamic processes in the track changes, Ertel's PV tendency budget is analyzed (see Huang et al. 2016b). For Ertel's PV defined by $q = (\boldsymbol{\omega}_a/\rho) \cdot \nabla\theta_v$, the prognostic equation of PV can be derived as

$$\frac{\partial q}{\partial t} = -\mathbf{U} \cdot \nabla q + \left(\frac{\boldsymbol{\omega}_a}{\rho} \cdot \nabla\right)\frac{d\theta_v}{dt} + \nabla\theta_v \cdot \frac{\nabla\rho \times \nabla p}{\rho^3}$$
$$+ \frac{1}{\rho}\nabla\theta_v \cdot (\nabla \times \mathbf{F}_r), \tag{A1}$$

where $\boldsymbol{\omega}_a = \boldsymbol{\omega} + 2\boldsymbol{\Omega}$ (using Earth rotation vector $\boldsymbol{\Omega}$ and the relative-vorticity vector $\boldsymbol{\omega} = \nabla \times \mathbf{U}$), $\mathbf{U}$ is the 3D wind vector (u, v, w), ρ is density, p is pressure, θ_v is the virtual potential temperature, and $\mathbf{F}_r = \tilde{\mathbf{F}}_r/\rho$ ($\tilde{\mathbf{F}}_r$ presents the turbulent mixing per unit mass in the momentum equation). The PV tendency budget terms on the right side of (A1) include the advection (both horizontal and vertical), diabatic heating, solenoidal effects and turbulent mixing effects. The diabatic heating term consists of three directional contributions, but the vertical contribution (i.e., the product of vertical absolute vorticity and vertical differential diabatic heating, mostly from latent heating), usually is dominant in the intense precipitation of a cyclonic typhoon. These budget terms averaged over 3–8 km height and 1 h are calculated on the height coordinates from the MPAS output. Solenoidal effects were found to be much smaller and are not presented in our results. Turbulent mixing effects above 3 km height are also very small and are not taken into account. For convenience, we interpolate the model variables to spherical coordinates with 0.025° spacing in latitude and longitude and 200 m spacing in height.

Based on the PV tendency budget, a regression method following Wu and Wang (2000) is utilized to estimate the east–west and north–south components of the typhoon translational speed given by

$$C_x = -\frac{\sum_{i=1}^{N}\left(\frac{\partial \overline{q}_0}{\partial x}\right)_i\left(\frac{\partial \overline{q}_1}{\partial t}\right)_i}{\sum_{i=1}^{N}\left(\frac{\partial \overline{q}_0}{\partial x}\right)_i^2}, \qquad C_y = -\frac{\sum_{i=1}^{N}\left(\frac{\partial \overline{q}_0}{\partial y}\right)_i\left(\frac{\partial \overline{q}_1}{\partial t}\right)_i}{\sum_{i=1}^{N}\left(\frac{\partial \overline{q}_0}{\partial y}\right)_i^2},$$
$$\tag{A2}$$

respectively, where the bar represents its vertical mean, indices 0 and 1 indicate the symmetric and WN-1 components, respectively, for any grid point i within a specified radius of the typhoon center. In this study, we choose the radius of 150 km for our analyses, which is close to 200 km width of a square area used by Hsu et al. (2018).

REFERENCES

Bender, M. A., R. E. Tuleya, and Y. Kurihara, 1987: A numerical study of the effect of an island terrain on tropical cyclones. *Mon. Wea. Rev.*, **115**, 130–155, https://doi.org/10.1175/1520-0493(1987)115<0130:ANSOTE>2.0.CO;2.

Chan, J. C., F. M. Ko, and Y. M. Lei, 2002: Relationship between potential vorticity tendency and tropical cyclone motion. *J. Atmos. Sci.*, **59**, 1317–1336, https://doi.org/10.1175/1520-0469(2002)059<1317:RBPVTA>2.0.CO;2.

Chang, S. W.-J., 1982: The orographic effects induced by an island mountain range on propagating tropical cyclones. *Mon. Wea. Rev.*, **110**, 1255–1270, https://doi.org/10.1175/1520-0493(1982)110<1255:TOEIBA>2.0.CO;2.

Davis, C. A., and S. Low-Nam, 2001: The NCAR-AFWA tropical cyclone bogussing scheme. Report for the Air Force Weather Agency (AFWA), 12 pp.

Fujiwhara, S., 1921: The natural tendency towards symmetry of motion and its application as a principle in meteorology. *Quart. J. Roy. Meteor. Soc.*, **47**, 287–292, https://doi.org/10.1002/qj.49704720010.

Hagos, S., R. Leung, S. A. Rauscher, and T. Ringler, 2013: Error characteristics of two grid refinement approaches in aquaplanet simulations: MPAS-A and WRF. *Mon. Wea. Rev.*, **141**, 3022–3036, https://doi.org/10.1175/MWR-D-12-00338.1.

Hsu, L.-H., H.-C. Kuo, and R. G. Fovell, 2013: On the geographic asymmetry of typhoon translation speed across the mountainous island of Taiwan. *J. Atmos. Sci.*, **70**, 1006–1022, https://doi.org/10.1175/JAS-D-12-0173.1.

——, S.-H. Su, R. G. Fovell, and H.-C. Kuo, 2018: On typhoon track deflections near the east coast of Taiwan. *Mon. Wea. Rev.*, **146**, 1495–1510, https://doi.org/10.1175/MWR-D-17-0208.1.

Huang, C.-Y., and Y.-L. Lin, 2008: The influence of mesoscale mountains on vortex tracks: Shallow-water modeling study. *Meteor. Atmos. Phys.*, **101**, 1–20, https://doi.org/10.1007/s00703-007-0284-1.

——, C.-S. Wong, and T.-C. Yeh, 2011: Extreme rainfall mechanisms exhibited by Typhoon Morakot (2009). *Terr. Atmos. Oceanic Sci.*, **22**, 613–632, https://doi.org/10.3319/TAO.2011.07.01.01(TM).

——, C.-A. Chen, S.-H. Chen, and D. S. Nolan, 2016a: On the upstream track deflection of tropical cyclones past a mountain range: Idealized experiments. *J. Atmos. Sci.*, **73**, 3157–3180, https://doi.org/10.1175/JAS-D-15-0218.1.

——, I.-H. Wu, and L. Feng, 2016b: A numerical investigation of the convective systems in the vicinity of southern Taiwan associated with Typhoon Fanapi (2010): Formation mechanism of double rainfall peaks. *J. Geophys. Res. Atmos.*, **121**, 12 647–12 676, https://doi.org/10.1002/2016JD025589.

——, Y. Zhang, W. C. Skamarock, and L.-F. Hsu, 2017: Influences of large-scale flow variations on the track evolution of Typhoons Morakot (2009) and Megi (2010): Simulations with a global variable-resolution model. *Mon. Wea. Rev.*, **145**, 1691–1716, https://doi.org/10.1175/MWR-D-16-0363.1.

Huang, Y.-H., C.-C. Wu, and Y. Wang, 2011: The influence of island topography on typhoon track deflection. *Mon. Wea. Rev.*, **139**, 1708–1727, https://doi.org/10.1175/2011MWR3560.1.

Jian, G.-J., and C.-C. Wu, 2008: A numerical study of the track deflection of Supertyphoon Haitang (2005) prior to its landfall in Taiwan. *Mon. Wea. Rev.*, **136**, 598–615, https://doi.org/10.1175/2007MWR2134.1.

Kuo, H.-C., R. T. Williams, J.-H. Chen, and Y.-L. Chen, 2001: Topographic effects on barotropic vortex motion: No mean flow. *J. Atmos. Sci.*, **58**, 1310–1327, https://doi.org/10.1175/1520-0469(2001)058<1310:TEOBVM>2.0.CO;2.

Lin, Y.-L., and L. C. Savage, 2011: Effects of landfall location and the approach angle of a cyclone vortex encountering a mesoscale mountain range. *J. Atmos. Sci.*, **68**, 2095–2106, https://doi.org/10.1175/2011JAS3720.1.

——, J. Han, D. W. Hamilton, and C.-Y. Huang, 1999: Orographic influence on a drifting cyclone. *J. Atmos. Sci.*, **56**, 534–562, https://doi.org/10.1175/1520-0469(1999)056<0534:OIOADC>2.0.CO;2.

——, S.-Y. Chen, C. M. Hill, and C.-Y. Huang, 2005: Control parameters for the influence of a mesoscale mountain range on cyclone track continuity and deflection. *J. Atmos. Sci.*, **62**, 1849–1866, https://doi.org/10.1175/JAS3439.1.

Liu, J. C., Y.-A. Liou, M.-X. Wu, Y.-J. Lee, C.-H. Cheng, C.-P. Kuei, R.-M. Hong, 2015: Analysis of interactions among two tropical depressions and Typhoons Tembin and Bolaven (2012) in Pacific Ocean by using satellite cloud images. *IEEE Trans. Geosci. Remote Sens.*, **53**, 1394–1402, https://doi.org/10.1109/TGRS.2014.2339220.

Park, S.-H., J. B. Klemp, and W. C. Skamarock, 2014: A comparison of mesh refinement in the global MPAS-A and WRF models. *Mon. Wea. Rev.*, **142**, 3614–3634, https://doi.org/10.1175/MWR-D-14-00004.1.

Sakaguchi, K., L. R. Leung, C. Zhao, Q. Yang, J. Lu, and S. Hagos, 2015: Exploring a multiresolution approach using AMIP simulations. *J. Climate*, **28**, 5549–5574, https://doi.org/10.1175/JCLI-D-14-00729.1.

Skamarock, W. C., and Coauthors, 2008: A description of the Advanced Research WRF version 3. NCAR Tech. Note NCAR/TN-475+STR, 113 pp., https://doi.org/10.5065/D68S4MVH.

——, J. B. Klemp, M. G. Duda, L. D. Fowler, S.-H. Park, and T. D. Ringler, 2012: A multiscale nonhydrostatic atmospheric model using centroidal Voronoi tesselations and C-grid staggering. *Mon. Wea. Rev.*, **140**, 3090–3105, https://doi.org/10.1175/MWR-D-11-00215.1.

Tang, C. K., and J. C. L. Chan, 2014: Idealized simulations of the effect of Taiwan and Philippines topographies on tropical cyclone tracks. *Quart. J. Roy. Meteor. Soc.*, **140**, 1578–1589, https://doi.org/10.1002/qj.2240.

——, and ——, 2015: Idealized simulations of the effect of local and remote topographies on tropical cyclone tracks. *Quart. J. Roy. Meteor. Soc.*, **141**, 2045–2056, https://doi.org/10.1002/qj.2498.

——, and ——, 2016: Idealized simulations of the effect of Taiwan topography on the tracks of tropical cyclones with different steering flow strengths. *Quart. J. Roy. Meteor. Soc.*, **142**, 3211–3221, https://doi.org/10.1002/qj.2902.

Wang, C.-C., H.-C. Kuo, Y.-H. Chen, H.-L. Huang, C.-H. Chung, and K. Tsuboki, 2012: Effects of asymmetric latent heating on typhoon movement crossing Taiwan: The case of Morakot (2009) with extreme rainfall. *J. Atmos. Sci.*, **69**, 3172–3196, https://doi.org/10.1175/JAS-D-11-0346.1.

——, Y.-H. Chen, H.-C. Kuo, and S.-Y. Huang, 2013: Sensitivity of typhoon track to asymmetric latent heating/rainfall

induced by Taiwan topography: A numerical study of Typhoon Fanapi (2010). *J. Geophys. Res. Atmos.*, **118**, 3292–3308, https://doi.org/10.1002/jgrd.50351.

Wang, S.-T., 1980: Prediction of the movement and strength of typhoons in Taiwan and its vicinity. National Science Council Research Rep. 108, Taipei, Taiwan, 100 pp.

Wu, C.-C., T.-S. Huang, W.-P. Huang, and K.-H. Chou, 2003: A new look at the binary interaction: Potential vorticity diagnosis of the unusual southward movement of Tropical Storm Bopha (2000) and its interaction with Supertyphoon Saomai (2000). *Mon. Wea. Rev.*, **131**, 1289–1300, https://doi.org/10.1175/1520-0493(2003)131<1289:ANLATB>2.0.CO;2.

——, T.-H. Li, and Y.-H. Huang, 2015: Influence of mesoscale topography on tropical cyclone tracks: Further examination of the channeling effect. *J. Atmos. Sci.*, **72**, 3032–3050, https://doi.org/10.1175/JAS-D-14-0168.1.

Wu, L., and B. Wang, 2000: A potential vorticity tendency diagnostic approach for tropical cyclone motion. *Mon. Wea. Rev.*, **128**, 1899–1911, https://doi.org/10.1175/1520-0493(2000)128<1899:APVTDA>2.0.CO;2.

——, and ——, 2001: Effects of convective heating on movement and vertical coupling of tropical cyclones: A numerical study. *J. Atmos. Sci.*, **58**, 3639–3649, https://doi.org/10.1175/1520-0469(2001)058<3639:EOCHOM>2.0.CO;2.

Wu, W., A. H. Lynch, and A. Rivers, 2005: Estimating the uncertainty in a regional climate model related to initial and lateral boundary conditions. *J. Climate*, **18**, 917–933, https://doi.org/10.1175/JCLI-3293.1.

Yang, C.-C., C.-C. Wu, K.-H. Chou, and C.-Y. Lee, 2008: Binary interaction between Typhoons Fengshen (2002) and Fungwong (2002) based on the potential vorticity dianosis. *Mon. Wea. Rev.*, **136**, 4593–4611, https://doi.org/10.1175/2008MWR2496.1.

Yeh, T.-C., and R. L. Elsberry, 1993a: Interaction of typhoons with the Taiwan topography. Part I: Upstream track deflections. *Mon. Wea. Rev.*, **121**, 3193–3212, https://doi.org/10.1175/1520-0493(1993)121<3193:IOTWTT>2.0.CO;2.

——, and ——, 1993b: Interaction of typhoons with the Taiwan topography. Part II: Continuous and discontinuous tracks across the island. *Mon. Wea. Rev.*, **121**, 3213–3233, https://doi.org/10.1175/1520-0493(1993)121<3213:IOTWTT>2.0.CO;2.

Yu, H., W. Huang, Y. H. Duan, J. C. L. Chan, P. Y. Chen, and R. L. Yu, 2007: A simulation study on pre-landfall erratic track of typhoon Haitang (2005). *Meteor. Atmos. Phys.*, **97**, 189–206, https://doi.org/10.1007/s00703-006-0252-1.

Zarzycki, C. M., and C. Jablonowski, 2015: Experimental tropical cyclone forecasts using a variable-resolution global model. *Mon. Wea. Rev.*, **143**, 4012–4037, https://doi.org/10.1175/MWR-D-15-0159.1.

——, ——, and M. A. Taylor, 2014: Using variable-resolution meshes to model tropical cyclones in the Community Atmosphere Model. *Mon. Wea. Rev.*, **142**, 1221–1239, https://doi.org/10.1175/MWR-D-13-00179.1.